Materials Science & Engineering A 792 (2020) 139798

Contents lists available at ScienceDirect

Materials Science & Engineering A

journal homepage: http://www.elsevier.com/locate/msea

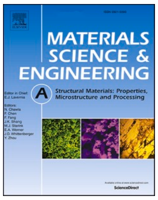

Novel intermetallic-reinforced near-α Ti alloys manufactured by spark plasma sintering

David Wimler [a,*], Janny Lindemann [b], Christoph Gammer [c], Petra Spoerk-Erdely [a], Andreas Stark [d], Helmut Clemens [a], Svea Mayer [a]

[a] Department of Materials Science, Montanuniversität Leoben, Roseggerstr. 12, 8700, Leoben, Austria
[b] GfE Fremat GmbH, Gewerbegebiet Süd 20, 09618, Brand-Erbisdorf, Germany
[c] Erich Schmid Institute of Materials Science, Austrian Academy of Sciences, Jahnstr. 12, 8700, Leoben, Austria
[d] Institute of Materials Research, Helmholtz-Zentrum Geesthacht, Max Planck-Str. 1, 21502, Geesthacht, Germany

ARTICLE INFO

Keywords:
Spark plasma sintering
Near-α alloy
α_2-Ti_3Al
Metal matrix composite
Microstructure
Mechanical properties

ABSTRACT

Near-α Ti alloys are ideal candidates for high-temperature aerospace, automotive and nautical propulsion systems due to their high strength, low density and good corrosion resistance. However, the maximum service temperature of the well-known near-α alloy Ti6242S is limited to about 540 °C. By adding, for example, intermetallic γ-TiAl based alloy particles to Ti6242S powder a significant increase in yield strength up to 650 °C can be achieved by means of spark plasma sintering, along with sufficient room temperature ductility. In this study, investigations on the underlying strengthening mechanisms were carried out. For this purpose, mechanical tests and detailed microstructural characterization were performed.

Spark plasma sintering at 1150 °C of powder blends with 10 m.% spherical γ-TiAl based powder (<20 μm) leads to a homogeneous dissolution of the TiAl particles in the matrix material and a refinement of the lamellar microstructure. Due to the formation of ordered intermetallic α_2-Ti_3Al precipitates, which are completely stable up to 670 °C in the newly evolved Ti-8.3Al-1.8Sn-3.7Zr-2.0Mo-0.9Nb-0.08Si alloy (m.%), the creep resistance at 600 °C has been increased significantly. In the B containing variant, it was found that finely distributed titanium borides TiB formed in the Ti6242 matrix and led to an even more pronounced refinement of the microstructure. For B additions of 1 m.%, however, the creep resistance at 600 °C is reduced compared to the other alloys, but the strength is increased up to 500 °C.

1. Introduction

The demand for light-weight structural components that endure high service temperatures has initiated a permanent development of new alloys as well as new processing routes. Presently, Ti-base alloys are used in structural high-temperature applications in the aerospace and automotive industries, as these alloys unite low density, high strength, and good corrosion and creep resistance at service temperature [1–5]. The common near-α Ti-base alloys (below 6 m.% Al) attain service temperatures below 600 °C, whereas intermetallic γ-TiAl-based alloys, which contain about 29–35 m.% Al (42–48 at.%), reach up to 800 °C with increasing creep, burn and oxidation resistance. TiAl alloys are already in use as turbine blades in advanced aircraft engines [6,7], valves in automotive engines [7,8] and turbocharger turbine wheels in automotive and nautical propulsion systems [5,8]. However, γ-TiAl alloys suffer from moderate ductility at room temperature (RT), which limits further applications [9,10].

Both, near-α Ti and γ-TiAl alloys are commonly produced by ingot metallurgy followed by hot deformation processes, e.g. forging or rolling, and subsequent multi-step heat treatments. However, powder-related processing routes provide the opportunity to manufacture complex near-net shapes, originating from pre-alloyed powder or powder blends. For example, the technique of spark plasma sintering (SPS) is quite a promising alternative to the conventional [1,4] and additive manufacturing (AM) technologies, e.g. see Ref. [11–14], of producing light-weight parts with high structural complexity like TiAl turbine

---

* Corresponding author.
E-mail addresses: david.wimler@unileoben.ac.at (D. Wimler), janny.lindemann@gfe.com (J. Lindemann), christoph.gammer@oeaw.ac.at (C. Gammer), petra.spoerk-erdely@unileoben.ac.at (P. Spoerk-Erdely), andreas.stark@hzg.de (A. Stark), helmut.clemens@unileoben.ac.at (H. Clemens), svea.mayer@unileoben.ac.at (S. Mayer).

https://doi.org/10.1016/j.msea.2020.139798
Received 6 May 2020; Received in revised form 17 June 2020; Accepted 18 June 2020

blades [15]. Thereby, SPS employs pulsed electric current and a uniaxial load to densify powders [15,16]. The use of powder facilitates the blending of Ti-base powder with other alloys or compounds into so-called titanium metal matrix composites (Ti-MMC), which exhibit enhanced mechanical properties after densification because of elements dissolution, grain refinement and/or dispersion strengthening [17–23]. For that reason, Ti-MMC components have already been introduced in the automotive industry as engine components, e.g. intake valves and exhaust valves [24].

This study investigates various powders and powder blends based on near-α Ti-base alloys densified via SPS. On the one hand, the matrix alloy Ti6242 with a nominal composition of Ti–6Al–2Sn–4Zr–2Mo (in m.%) was reinforced with B, and on the other hand, the advanced Ti–6Al–2Sn–4Zr–2Mo-0.1Si (in m.%) (Ti6242S) alloy was strengthened with particles of an intermetallic γ-TiAl based alloy, the so-called TNM alloy, with a nominal composition of Ti-43.5Al–4Nb–1Mo-0.1B (in at.%) (Ti-28.6Al–9Nb-2.3Mo-0.03B in m.%). The densification of commonly available powder or powder blends in the SPS unit opens up a fast and independent way of processing Ti-base alloys with advanced mechanical properties.

In general, many Ti-base alloys utilize the occurrence of two phases: the body-centered cubic (bcc) β-Ti (A2 structure) and the hexagonal close-packed (hcp) α-Ti (A3 structure), whereby the α-Ti is not thermodynamically stable above the allotropic transformation temperature, the so-called β transus temperature ($T_{\beta,trans}$). Below $T_{\beta,trans}$ both phases can appear, whereby the α/β ratio is determined by the chemical composition of the Ti-base alloy. For instance, Al and O are strong α stabilizers and therefore increase the amount of α phase in the microstructure, whereas Sn and Zr are considered to be weak α stabilizers. In contrast, Mo and Nb are β stabilizers, as they increase the β phase fraction, whereby Mo has an approximately four times stronger effect than Nb [4].

In this regard, Ti-base alloys are classified conventionally according to their equilibrium phase constitution, which consequently depends on the chemical composition [1–4]. The Ti6242 alloys belong to the near-α Ti alloys because the majority of the microstructure consists of the hcp α phase, which is appropriate for creep resistant high-temperature applications due to its low self-diffusion coefficient and its low number of dislocation slip systems when compared to the bcc β phase [1]. The addition of the β-eutectic element Si [1,4], which results in the so-called Ti6242S alloy, improves the mechanical properties at elevated temperatures by solution strengthening and the formation of stable intermetallic $(Ti,Zr)_5Si_3$ precipitates ($D8_8$-structure) at the α/β lamellae boundaries and at grain boundaries [25–27], which retard dislocation movement in comparison to the Si-free Ti6242 variant [1,25]. Additional strengthening in Ti-base alloys can be reached, e.g. due to the addition of Sn, by increasing the volume fraction of the intermetallic, ordered hexagonal α_2-Ti_3Al phase ($D0_{19}$ structure), since coherent precipitates are effective barriers for dislocation glide and climb [4]. The α_2-Ti_3Al phase precipitates from its disordered counterpart α during a final annealing treatment, resulting in an age-hardening effect by these fine α_2 precipitates. This aging step has to take place below the α_2 solvus temperature ($T_{\alpha2,solv}$). Aging or the application above $T_{\alpha2,solv}$ will dissolve the α_2 precipitates and thus the age-hardening effect will be lost, while limiting the maximum service temperature of this type of Ti-base alloys. The occurrence of this ordering transformation depends on the chemical composition of the alloy. For Ti6242S, where the long-term service temperature is set at 540 °C [28], $T_{\alpha2,solv}$ is about 650 °C according to literature [4,29]. The presence of O [29], Sn [4] or a further increase of the Al content [2,4,29] in Ti-base alloys promotes the formation of the intermetallic, ordered hexagonal α_2 phase, i.e. $T_{\alpha2,solv}$ and hence the service temperature is increased.

Based on the size and arrangement of the two major phases, α and β, a variety of microstructures is adjustable, which is reflected in the material's mechanical properties. The highest service temperatures are reached when near-α Ti alloys exhibit a fully lamellar (FL) microstructure, which consists mainly of lamellar α separated by retained β phase [2,4]. Therefore, a heat treatment above $T_{\beta,trans}$, in the single β phase field region, is conducted followed by cooling to RT; here, β transforms to α, obeying the Burgers orientation relationship: $(110)_\beta \parallel (0002)_\alpha$ and $[1\bar{1}1]_\beta \parallel [11\bar{2}0]_\alpha$ [30]. The cooling rate from the β phase field region defines the extent of this first transformation reaction, which forms in the case of slow cooling a continuous α layer at the boundary of the parent β grain, the so-called α seam. The cooling rate also determines the width of the next transforming α lamellae and the size of the α colonies.

During annealing above $T_{\beta,trans}$, the coarsening of the β grains can be inhibited by the presence of a second phase, such as TiB or TiC. Furthermore, adding borides and carbides into the metal matrix (e.g. as shown by Lu et al. [17] in the case of Ti6242S) results in a more fine-grained starting microstructure due to the fine particles which act as heterogeneous nucleation sites. As a consequence, the yield strength at room temperature is increased due to the combined strengthening effect of dispersoid and precipitate particles together with the finer grain size. Recent tensile tests of Ti–6Al–4V/(TiC + TiB)-MMCs up to 650 °C revealed a superior tensile strength at RT with a degradation around 600 °C [31]. However, tensile and creep test results at elevated temperatures for Ti6242/(TiB)-MMCs have not been published so far. The addition of intermetallic γ-TiAl alloy particles to a Ti-base alloy was reported first by Decker et al. [32,33]. These authors showed that the addition of 10–20 m.% of TNM powder increases the strength significantly at the expense of RT ductility, using Ti–6Al–4V [33] and Ti6242S [32] powder as matrix material densified via SPS. In case of the Ti6242S matrix, the addition of 10 m.% TNM particles smaller than 20 μm were considered to be an optimum in increasing strength but maintaining ductility as reported in Ref. [32] and was therefore chosen to be investigated in more detail. The present paper will clarify the strengthening mechanisms activated in Ti6242S reinforced with TNM powder particles and B at RT and elevated temperatures by using high-resolution electron microscopy along with ex situ and in situ X-ray diffraction. Finally, tensile and creep tests show the potential of the newly-designed Ti-MMCs and alloys for their use at 600 °C.

2. Materials and methods

All powders used were gas atomized employing argon inert gas and subsequently classified by sieving. The Ti6242S powder (10–106 μm) was atomized by LPW Technology Ltd, UK, and the TNM powder (<20 μm) by the Helmholtz-Zentrum Geesthacht, Germany. The pre-alloyed Ti6242 powder containing 1 m.% B (150–500 μm) was provided by Carpenter Technology (formerly Puris), USA. The Ti6242S + 10 m.% TNM powder blend was mixed under argon atmosphere via a shaker mixer Turbula T2 C from the WAB Group, Switzerland. The chemical compositions of the powders were determined by means of X-ray fluorescence (XRF) spectroscopy for Ti, Al, Nb, and Mo. Inductively coupled plasma-atomic emission spectroscopy (ICP-AES) was employed for B and Si. To analyze the interstitial O impurities, carrier gas hot extraction was employed. The composition of the powder blend after densification by SPS was determined with the same methods. The results are summarized in Table 1.

The powders and their blends were compacted to cylindrical samples with a diameter of 80 mm and a height of 14 mm by an SPS device of the type HP D 25 from FCT Systems GmbH, Germany, at the Technische Universität Bergakademie Freiberg, Germany. The densification of the powder was reached under vacuum by applying mechanical pressure and pulsed electric current. For more details regarding the SPS process, the reader is referred to Ref. [15,16,34]. The powders used in this study were sintered with different parameters, i.e. varying dwell temperature and dwell time, which are collectively shown for each condition in Table 2. All samples were cooled to RT at a rate of about 90 K/min, within the SPS unit via natural convection cooling. The dense samples in

Table 1
Chemical composition of the powder alloys and their blends evaluated either at the initial state or after SPS. The composition of the blend was calculated from the ingredients as well.

Variant		Elements [m.%]								
		Ti	Al	Sn	Zr	Mo	Si	Nb	B	O
Ti6242S[a]	Powder	bal.	6.00	2.04	3.98	2.03	0.08	–	–	0.19
Ti6242 + 1 m.% B[a]	Powder	bal.	6.28	1.84	4.26	1.84	–	–	1.010	0.11
TNM[a]	Powder	bal.	28.6	–	–	2.30	–	9.1	0.025	0.15
Ti6242S + 10 m.% TNM[a]	SPS	bal.	8.26	1.81	3.72	2.04	0.08	0.9	0.005	0.19
Ti6242S + 10 m.% TNM[b]	Blend	bal.	8.26	1.80	3.60	2.03	0.07	0.9	0.003	0.18

[a] Chemical analysis.
[b] Calculated.

Table 2
SPS process parameters used for each investigated variant. All variants were heated to their dwell temperature with 50 K/min under an applied load of 50 MPa. After the dwell time, the samples were cooled via natural convection with about 90 K/min.

Variant	Spark plasma sintering	
	Dwell temperature	Dwell time
Ti6242S	1100 °C	0 min
Ti6242 + 1 m.% B	1200 °C	3 min
Ti6242S + 10 m.% TNM 1100 °C	1100 °C	0 min
Ti6242S + 10 m.% TNM 1150 °C	1150 °C	0 min

as-SPS condition were metallographically examined by light optical microscopy (LOM) and scanning electron microscopy (SEM). To this end, specimens were taken from the center of the SPS disc, embedded into the hot mounting resin PolyFast from Struers, Germany, ground and subsequently either polished for 10 min, using a colloidal silica solution (OP–S suspension) from Struers, Germany, or etched in Kroll's reagent [35] for 8 s. All LOM images were recorded employing a Zeiss Axio Imager M1m, Germany. The SEM investigations were conducted on an EVO 50 from Zeiss, Germany, in back-scattered electron (BSE) mode at a maximum acceleration voltage of 20 kV. Energy-dispersive X-ray spectroscopy (EDX) was performed at a Tescan SEM of the type CLARA, Czech Republic, with an acceleration voltage of 15 kV in combination with the X-Max system and the Aztec software from Oxford Instruments, United Kingdom.

X-ray diffraction (XRD) measurements were conducted on OP-S polished samples using Cu K_α radiation in an AXS D8 Advanced diffractometer from Bruker, United States. The data obtained and the corresponding Rietveld refinement [36] were used to identify the appearing phases and evaluate the phase fractions with an accuracy of ±3 m.%, applying the software program TOPAS from Bruker, United States. High-energy X-ray diffraction (HEXRD) experiments were conducted at the side station P07B of the high-energy materials science (HEMS) beamline operated by the Helmholtz-Zentrum Geesthacht at PETRA III at the Deutsches Elektronen-Synchrotron (DESY) in Hamburg, Germany [37]. During the experiments on cylindrical samples (Ø5 × 10 mm^3), 2D diffraction patterns were continually collected in transmission geometry using a PerkinElmer XRD 1621 flat panel detector with a pixel matrix of 2048 × 2048 and a pixel size of 200 × 200 μm^2. A mean photon energy of 87.1 keV was selected corresponding to a wavelength of 0.1424 Å. The experimental setup was calibrated with LaB_6 powder. The recorded Debye-Scherrer rings were azimuthally integrated using the data reduction software program Fit2D [38]. Besides RT measurements, in situ HEXRD phase evolution experiments were conducted using a modified quenching and deformation dilatometer DIL805A/D from TA Instruments (formerly Bähr Thermoanalyse GmbH), Germany. Samples in as-SPS condition were heated up to 500 °C and held for 30 min. Afterwards, the temperature was increased to 1150 °C at a heating rate of 2 K/min. An exposure time of 2 s per image provided an adequate peak-to-background intensity ratio during the experiments. Phase fractions and their dependence on time and temperature were evaluated by the intensity ratio method [39,40]. Weighting factors were derived from the results of Rietveld analysis, which was performed for selected temperatures. The appearance of upper harmonics at P07B has been considered in the evaluation.

In order to analyze transformation sequences, differential scanning calorimetry (DSC) measurements were carried out on SPS samples, utilizing heating rates between 10 and 40 K/min in Ar-atmosphere. The measurements were executed on a LabSYS Evolution of Setaram Instrumentation, France, whereby the weight of the specimens was around 45 ± 5 mg, and the specimens were enclosed by a 100 µl alumina crucible. The samples tested were homogenized at 1150 °C for 4 h in a vacuum furnace ($5 \cdot 10^{-6}$ mbar) from HTM-Reetz, Germany, prior to the DSC experiments.

Quasi-static tensile tests were carried out at RT, 300 °C, 450 °C, 550 °C, 600 °C, and 650 °C at a strain rate of 10^{-4} s^{-1} on universal testing machines of the type Inspect 50–1 from Hegewald and Peschke, Germany, and AG-100 from Shimadzu, Japan, according to DIN EN ISO 6892–1. At maximum two specimens were tested at each temperature. The tensile and creep test specimens were eroded from the sintered discs by electrical discharge machining. The final tensile test samples had a diameter of 5 mm and a gauge length of 25 mm. The creep samples had a diameter of 6 mm and a gauge length of 30 mm. The creep tests were performed at a temperature of 600 °C under an applied load of 210 MPa, employing AET Technologies', France, TC30 and TC50 creep testing machines. Extensometer bars were used to determine the creep strain. Stable thermal conditions along the gauge length were guaranteed through three attached thermocouples, monitoring and controlling the temperature.

Transmission electron microscopy (TEM) investigations were carried out on a JEOL JEM-2200FS, Japan, operating at 200 kV. The samples (3 mm in diameter) were electrolytically thinned to electron transparency using a Tenu Pol-5 and the electrolyte A3 from Struers, Germany.

3. Results

3.1. Microstructure

After spark plasma sintering of the different powders according to Table 2, the etched as-SPS samples were investigated by means of LOM. Ti6242S powder was sintered above $T_{\beta,trans}$, which is about 1000 °C for this alloy according to Ref. [3]. Additionally, DSC measurements on the SPS sample determined $T_{\beta,trans}$ to be 1006 ± 5 °C. The adjusted microstructure is shown in Fig. 1a. The employed dwell temperature of 1100 °C leads to coarse β grains, whose grain boundaries are still visible through the enclosing α seam. This α seam at the former grain boundaries of the parent β grains is generated firstly while cooling, followed by the formation of several differently oriented α colonies within each β grain. Due to the cooling rate of about 90 K/min, as achieved in the SPS unit for the present sample dimensions, the α seam, the α colonies and the single α lamellae are coarse and, therefore, visible in the LOM image.

As shown in Fig. 1b, the addition of 1 m.% B drastically refines the

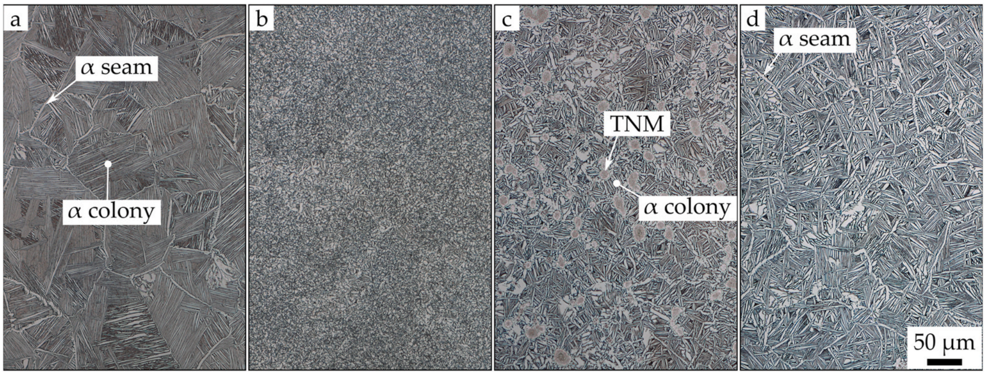

Fig. 1. LOM images of the Kroll etched specimens in as-SPS condition: a) Ti6242S; b) Ti6242 + 1 m.% B; c) Ti6242S + TNM, dwell temperature 1100 °C and d) Ti6242S + TNM, dwell temperature 1150 °C. a) The former β grains are apparent by the enclosing α seam. Parallel-oriented α-Ti lamellae are within the α colonies, which obviously nucleate at the α seam. b) A refined microstructure is visible when compared to a). c) The spherical TNM particles are recognizable between the refined colonies. d) All spherical TNM particles were dissolved into the Ti6242S matrix and the microstructure coarsened when compared to c) and a distinct α seam is again discernible (see text).

microstructure due to the tendency of B to form intermetallic Ti borides which are already present in the powder. These borides act as heterogeneous nucleation sites for β in the melt, e.g. during gas atomization, and throughout the subsequent solid-state phase transformations, i.e. during the SPS process. Heterogeneous nucleation at Ti borides was already utilized for Ti–6Al–4V [17] and γ-TiAl alloys [41,42] and confirms the observed refined microstructure.

The powder blends containing 90 m.% Ti6242S and 10 m.% TNM are sintered at two different temperatures according to Table 2. At 1100 °C the TNM powder particles are totally embedded in the Ti6242S matrix, but still visible in the LOM image of Fig. 1c. The α colonies are significantly smaller than those of the Ti6242S microstructure in Fig. 1a. The finer colonies are attributed to the pinning of the β grain boundaries by TNM particles during sintering above $T_{\beta,trans}$. Furthermore, no enclosing α seam is apparent. Thus, it can be concluded that the α formation starts rather at the TNM particles than at the β grain boundaries.

Increasing the sintering temperature to 1150 °C leads to the dissolution of the TNM particles, which is shown in Fig. 1d and correlates with data from Decker et al. [32]. At this temperature the grain size could be kept small when compared to Ti6242S in Fig. 1a, even though the TNM particles have dissolved. The observed effect is caused by the grain boundary pinning before the TNM particles have fully vanished. Afterwards, the short process time of SPS impedes grain coarsening. However, when compared to Fig. 1c, the colony size is slightly larger and the α seam is again present at former β grain boundaries, facilitating the nucleation of colonies whose size is still refined when compared to the basic Ti6242S as-SPS microstructure, as shown in Fig. 1a.

In the next section, a more detailed investigation of the as-SPS samples was conducted. Therefore, SEM images were taken in BSE mode. As shown in Fig. 2a, the microstructure of the Ti6242S specimen contains the retained β phase (bright contrast) which either separates the parallel arranged α lamellae (gray) within a colony or in between these colonies. Spot EDX measurements on the α and β phase confirm the tendency of Al to accumulate in α, whereas Mo as well as Zr partition to the β phase, as does Sn, albeit to a lesser extent. The quantitative EDX results are presented in Table 3. The Al and Mo distributions agree with ref. [4], but in case of Zr and Sn the enrichment is contrary to literature, where enrichment in the α phase would be expected [4].

A comparable microstructure can be seen in Fig. 2b for the Ti6242S alloy, where TNM particles were added and the blend was sintered at 1100 °C (see Table 2). The TNM particles are still visible in the SEM image, appearing spherical and dark contrasted in BSE mode due to the

Table 3
Chemical composition of the phases and target areas determined by spot or area EDX measurements.

Variant	Phase or area	Elements [m.%]						
		Ti	Al	Sn	Zr	Mo	Si	Nb
Ti6242S	α	bal.	6.7	2.0	3.9	0.7	<0.2	–
	β	bal.	4.0	2.6	6.5	7.7	<0.2	–
Ti6242S + 10 m.% TNM 1100 °C	α	bal.	7.9	2.3	3.8	0.4	<0.2	0.0
	β	bal.	5.7	2.1	5.9	6.0	<0.2	1.5
	TNM particle	bal.	28.0	<0.2	<0.2	2.4	<0.2	9.1
Ti6242S + 10 m.% TNM 1150 °C	α	bal.	8.7	1.9	3.4	0.5	<0.2	0.5
	β	bal.	5.6	2.4	5.3	8.0	<0.2	1.4
	Area scan	bal.	8.0	2.0	4.1	2.2	<0.2	0.8

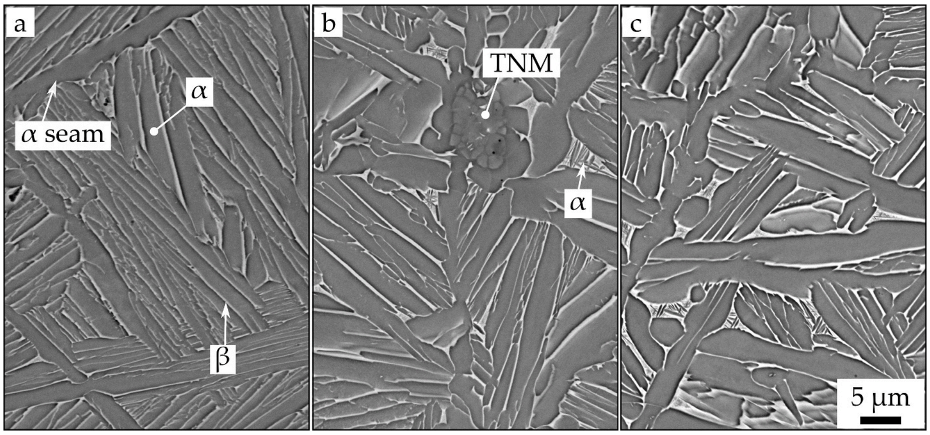

Fig. 2. SEM images of Kroll etched SPS samples taken in BSE mode: a) Ti6242S, b) Ti6242S + TNM, dwell temperature 1100 °C and c) Ti6242S + TNM, dwell temperature 1150 °C. a) The Ti6242S microstructure consists of gray contrasted α-Ti lamellae surrounded by the bright β phase. b) Inside the coarser β grains, fine α platelets are visible (as indicated). Similar α platelets can be seen in c), but without the presence of TNM particles.

higher Al content of the TNM alloy surrounded by gray α phase. EDX measurements on the α and β phase close to the TNM particle as well as on the TNM particle are summarized in Table 3. The Al content in both phases, α and β, is increased when compared to Ti6242S, confirming that the TNM particles already started to dissolve in the matrix. However, the center of the TNM particles still has its original composition (compare Tables 1 and 3). When comparing the microstructure of the pure Ti6242S in Fig. 2a with the sintered blend in Fig. 2b, expanded β phase areas, containing fine α phase, are visible. These α platelets harden the β phase, which results in an improvement of the mechanical properties as already reported for the Ti–6Al–4V alloy [29]. A similar α microstructure is adjusted in expanded β phase areas by sintering the Ti6242S + TNM blend at 1150 °C, see Fig. 2c. All TNM powder particles have homogeneously dissolved into the matrix, whereby Al further accumulates in the α phase, whereas Nb and Mo are enriched in the β phase, as seen in Table 3. An EDX area scan yielded a chemical composition of Ti-8.0Al-2.0Sn-4.1Zr-2.2Mo-0.8Nb, which is in agreement with the values in Table 1, demonstrating the accuracy of the EDX quantification for these elements.

The pre-alloyed Ti6242 + 1 m.% B powder was sintered at 1200 °C for 3 min, resulting in the microstructure shown in Fig. 3. The microstructure consists of black Ti borides and gray α phase surrounded by bright β phase. The α phase appears globular and no longer attains the shape of lamellar colonies. The α grain size is significantly smaller when compared to the pure Ti6242S alloy shown in Fig. 1a. During the sintering at 1200 °C, the borides prevent an extensive growth of the β grains above $T_{\beta,trans}$ and act as heterogeneous nucleation sites during heating and cooling. Therefore, the B-containing microstructure represents the finest one of all the investigated microstructures. Qualitative spot EDX measurements on the acicular, black-appearing phase confirmed the presence of finely dispersed Ti borides. A quantitative determination of the light element B was not possible.

3.2. X-ray diffraction

The samples in as-SPS condition were investigated by means of XRD to identify the phases appearing in the microstructure as well as to determine their phase fraction at RT. In Fig. 4 diffraction patterns are shown where the intensity is plotted logarithmically as a function of the 2θ angle along with the peak positions of α, α_2, β, and TiB. The top graph (red color) shows the spectrum of Ti6242S serving as a reference, where α and β peaks are identified. The application of Rietveld refinement resulted in 90 m.% α phase and 10 m.% β phase. The weak peaks at 41.5° and 54.0° occur in any XRD pattern in Fig. 4 and could not be assigned to any mentioned phase. However, the HEXRD measurement discussed below does not show such peaks, which is why they are neglected in the following discussion.

The next graph (blue) was obtained for a Ti6242 sample containing 1 m.% B. Rietveld refinement resulted in 89 m.% α phase and 11 m.% β phase by taking only these two phases into account. However, the XRD intensity spectrum also exhibits peaks that belong to orthorhombic TiB (B27 structure [9]), e.g. at 29.2° or 46.5°. These peaks confirm the presence of Ti borides, also detected in the SEM micrograph (Fig. 3) and associated EDX measurement. Due to their low phase fraction and orthorhombic structure, their peak-to-background ratio is too weak for quantitative Rietveld analysis. The peak positions, however, fit the indicated orthorhombic B27 structure, rather than the hexagonal TiB_2 structure, which could be taken next into consideration [9,19]. Supposing that each B atom in the alloy forms a monoboride together with one Ti atom, while Ti has 4.4 times the molar mass of B, 1 m.% boron in our alloy should result in 5.4 m.% TiB.

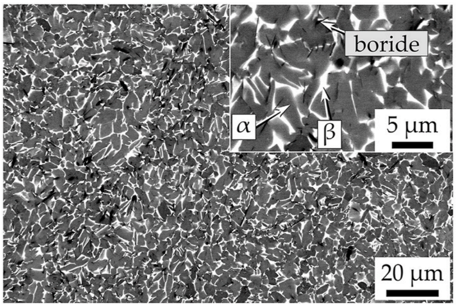

Fig. 3. SEM images of OP-S polished specimens in BSE mode: Ti6242 + 1 m.% B, whereby the insert shows microstructural details at a higher magnification. The acicular phase is identified as TiB, which appears dark in the BSE contrast. The SEM image shows finely dispersed borides in a fine globular microstructure.

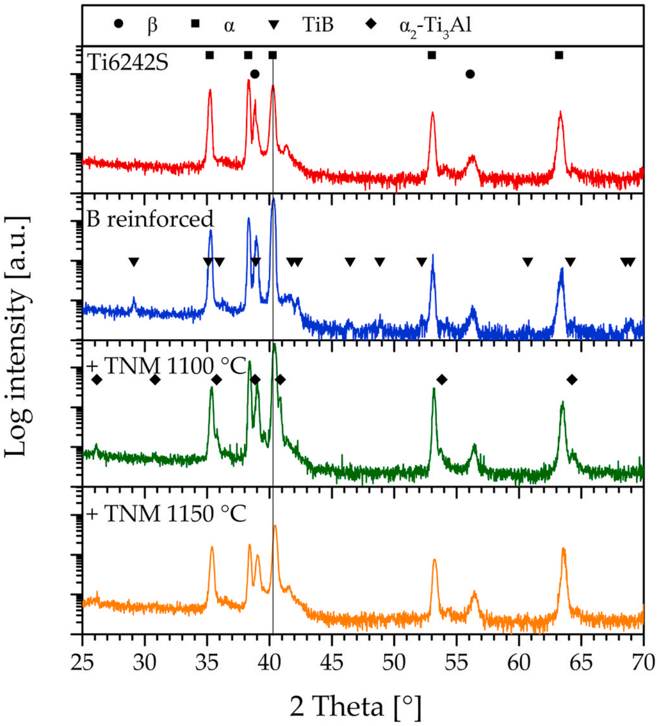

Fig. 4. XRD intensity spectrum (logarithmic intensity scale) of four samples in as-SPS condition. Due to different powder blends and sinter temperatures in use, different phases can be identified (see text).

The third graph from the top (green) in Fig. 4 shows the intensity spectrum of Ti6242S which contains 10 m.% TNM powder particles and was sintered at 1100 °C, i.e. the blend for which a complete dissolution of the TNM particles has not yet been achieved. The spectrum reveals additional peaks, e.g. at 26.1°, 35.8°, 40.9°, 53.7° and 64.1°, belonging to the α_2 phase. Since both α and its ordered counterpart α_2 show a hexagonal crystal structure, superlattice peaks, such as at 26.1°, are a clear indication of the existence of the α_2 phase [43]. The other α_2-peaks can be found on the right side of the corresponding α peaks, which is due to a slightly different hexagonal lattice when compared to the disordered α phase, including the chemical heterogeneity of undissolved TNM particles. The α peaks are also shifted to higher 2θ angles, e.g. from 40.38° in Ti6242S (marked with a vertical line in Fig. 4) to 40.42° in the Ti6242S + TNM 1100 °C variant. In the TNM-containing sample this is caused by elements stemming from already dissolved TNM powder particles which in turn change the lattice parameters. The β phase fraction is 8 m.%. An exact differentiation between the α and α_2 phase fraction cannot be made and therefore their fraction adds up to 92 m.%.

The bottom graph in Fig. 4 shows the same Ti6242S + TNM blend sintered at 1150 °C, leading to a total dissolution of the TNM particles. In the spectrum, the superlattice of α_2 peak is barely detectable at 26.1°. When compared to the specimen sintered at 1100 °C, no additional α_2

peaks can be found on the right side of the α peaks. It is concluded that both α and α_2 exhibit a hexagonal lattice with similar lattice parameters, due to a homogeneous distribution of the elements. A separation into α and α_2 phase fractions is also not possible. Their collective phase fraction was therefore summed up to 91 m.%. The remaining phase fraction is attributed to the β phase. Again, a peak shift to higher 2θ angle can be identified when comparing with the α peaks of the Ti6242S variant (marked with a vertical line). The shift is a consequence of the change in the lattice parameter by additional elements. The corresponding lattice volume of the hexagonal α phase was evaluated, and this resulted in a reduction of the unit-cell volume by 1% owing to the dissolution of the TNM particles. Yet at the same time, the α/α_2 and β phase fractions stay at 90 ± 3 and 10 ± 3 m.%, respectively, for all variants.

3.3. High-energy X-ray diffraction

First, for the sake of comparison, HEXRD experiments were conducted on Ti6242S and Ti6242S + TNM 1150 °C samples in the as-SPS condition at RT. Rietveld analyses of both samples resulted in $\alpha/\alpha_2 = 90 \pm 2$ and $\beta = 10 \pm 2$ m.%, and the unit cell volume of α was found to decrease by roughly 1% in the course of dissolving the TNM particles. The α_2 phase could be detected in the as-SPS condition of Ti6242S + TNM 1150 °C, but not in the Ti6242S variant. These results confirm those provided in chapter 3.2. However, despite the high brilliance of the synchrotron beam and the good peak-to-background ratio, the respective contribution of α and α_2 could not be measured quantitatively.

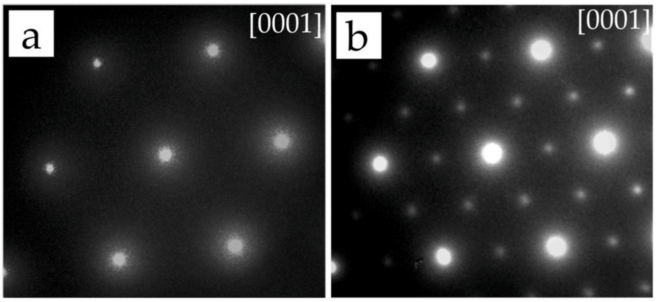

Fig. 6. Phase fraction diagram of the Ti6242S + TNM 1150 °C sample with the chemical composition of Ti-8.3Al-1.8Sn-3.7Zr-2.0Mo-0.9Nb-0.08Si (m.%), including relevant temperatures (see text).

Secondly, besides RT experiments, in situ heating HEXRD experiments were also conducted. Therefore, a Ti6242S + TNM 1150 °C sample in as-SPS condition was heated to 1150 °C. The intensity plot in Fig. 5a confirms the presence of α, α_2 and β at 500 °C, whereby the α/α_2 fraction is 90 ± 2 m.% and the remaining 10 ± 2 m.% phase is β. When increasing the temperature, first the α_2 peaks vanish. This behavior can be observed most distinctly by tracing the α_2 superlattice reflections at small 2θ angles. Upon further heating, also the α reflections vanish for the benefit of β. To quantitatively determine the α_2 solvus temperature $T_{\alpha2,solv}$ as well as the β transus transformation temperature $T_{\beta,trans}$, Fig. 5b shows the summed intensity of selected α_2 superlattice reflections ($10\bar{1}1$ and $11\bar{2}0$, black curve) and fundamental peaks (α: $10\bar{1}0$, $10\bar{1}1$ and $10\bar{1}2$, green curve). The intensity of α_2 starts to increase at roughly 600 °C, reaching a maximum at 670 °C ($T_{\alpha2,max}$). Consequently, the α_2 phase was not precipitated entirely from α in the as-SPS condition, and further ordering was promoted by an increase in temperature during the HEXRD experiment. Above 670 °C, the α_2 intensity and, thus, its phase fraction decreases. It drops below 1% of the intensity maximum at 1005 °C, which is set as $T_{\alpha2,solv}$. The α solvus temperature, which equals $T_{\beta,trans}$, was determined as 1060 °C. This result is in accordance with the DSC measurements, which found $T_{\beta,trans}$ to be 1054 ± 7 °C. Note, when $T_{\beta,trans}$ is exceeded, a single phase field region is reached, and thus grain growth occurs during further heating, which can also be recognized by

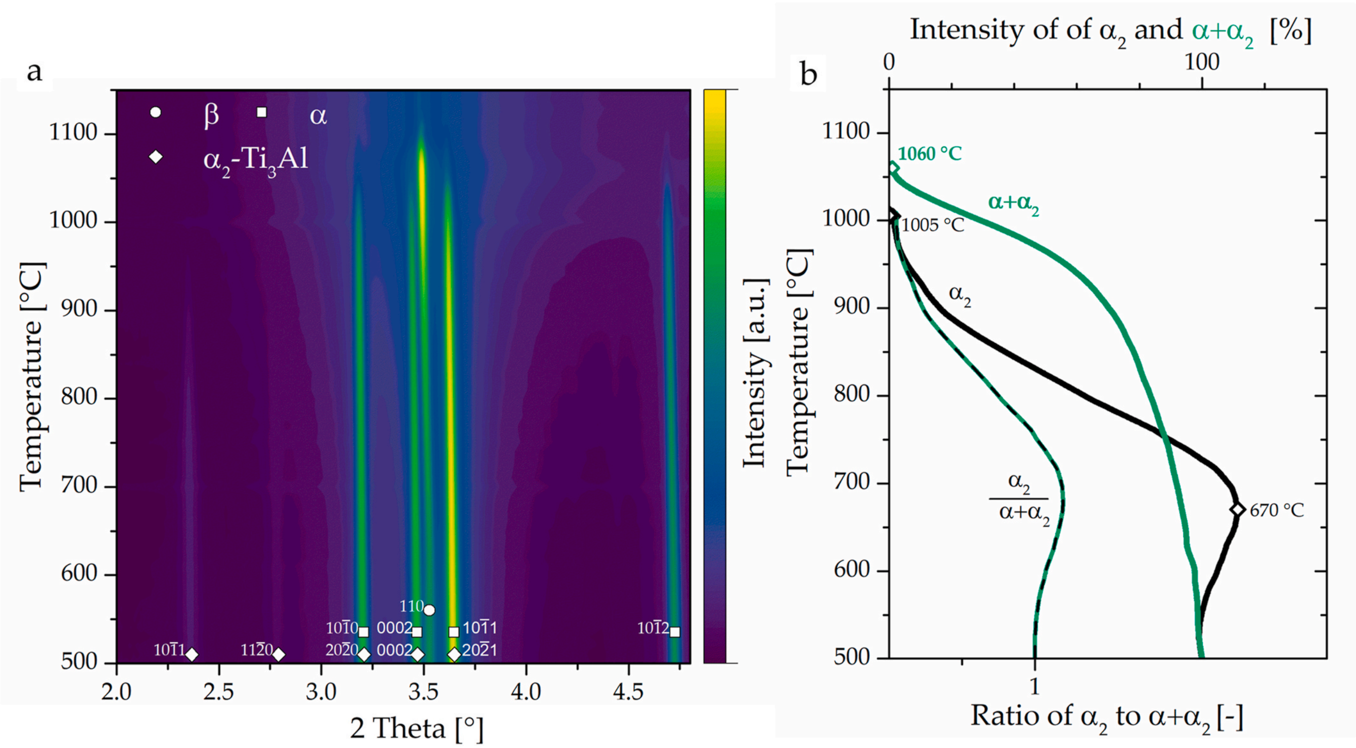

Fig. 5. In situ HEXRD measurement on the Ti6242S + TNM 1150 °C sample in as-SPS condition. a) The measured intensity is plotted logarithmically, showing α, α_2 and β at 500 °C. b) The intensity of α_2 superlattice reflections and $\alpha+\alpha_2$ fundamental reflections as well as their ratio as a function of the temperature, where intensity values are normalized to the intensity observed at 500 °C. The solvus temperatures of α_2 and α were determined to be 1005 and 1060 °C, respectively, where the intensity decreased to 1% of its maximum value.

the decreasing intensity of the β peaks in Fig. 5a. Finally, the ratio between the α_2 and α+ α_2 intensities is also shown in Fig. 5b. As discussed above, the change in the ratio points out that both α_2 and α are present side by side and their respective phase fraction increases or decreases at the expense of the other in the course of ordering or disordering transformations. Otherwise the ratio would be constant.

Based on the HEXRD intensities of the Ti6242S + TNM 1150 °C sample, the phase fractions of α/α_2 (collective amount) and β were evaluated as a function of the temperature and plotted in Fig. 6. In addition, the transformation temperature, mentioned above were marked for further discussions.

3.4. Transmission electron microscopy

In order to examine the appearance of the ordered α_2-Ti_3Al phase in the microstructure, TEM investigations were conducted on a Ti6242S and a Ti6242S + 10 m.% TNM 1150 °C specimen in as-SPS condition. Diffraction patterns (DP) can disclose the presence of the ordered α_2 due to superlattice reflections, which would be missing in the case of a completely disordered hexagonal α phase [44,45]. Fig. 7a and b show DP of a Ti6242S and a Ti6242S + TNM 1150 °C sample, respectively, in as-SPS condition tilted in the same [0001] zone axis. This comparison clarifies that in the Ti6242S sample, the α-phase is completely disordered due to missing superlattice reflections. Conversely, in Ti6242S + 10 m.% TNM 1150 °C in as-SPS condition, where the superlattice reflections are located between the regular hexagonal reflections, the α_2 phase is present. Therefore, a detailed microstructural investigation was conducted on this specimen, as shown in Fig. 8. Fig. 8a shows a high angle annular dark field (HAADF) scanning transmission electron microscopy (STEM) image of an α/β colony. The HAADF STEM provides an atomic number (Z) contrast, i.e. the heavier the elements in the phase, the brighter the phase appears in the image [46]. As a result, the β phase, which is enriched in heavy elements such as Mo and Nb, appears in bright contrast, whereas the Al-enriched α phase appears in dark contrast. Inside the bright β phase, no contrast differences are detectable, so no additional α phase has formed in the fine, retained β lamellae. This is in contrast to extended β phase areas, as analyzed in Fig. 2c. Selective area diffraction (SAD) was conducted on the α phase. The corresponding DP again discloses the presence of the ordered α_2 due to superlattice reflections. The insert in Fig. 8b shows the DP of a selected area taken in $[1\bar{2}1\bar{3}]$ zone axis. By using the $10\bar{1}1_{\alpha2}$ superlattice reflection, a dark field (DF) image was taken, shown in Fig. 8b. The illuminated areas are ordered domains (OD) of α_2 phase, whereas the disordered areas remain dark. The size of the OD is below 10 nm and they occupy almost the entire grain, occasionally only separated by anti-phase boundaries (APB), appearing as dark contrasted lines in the DF image.

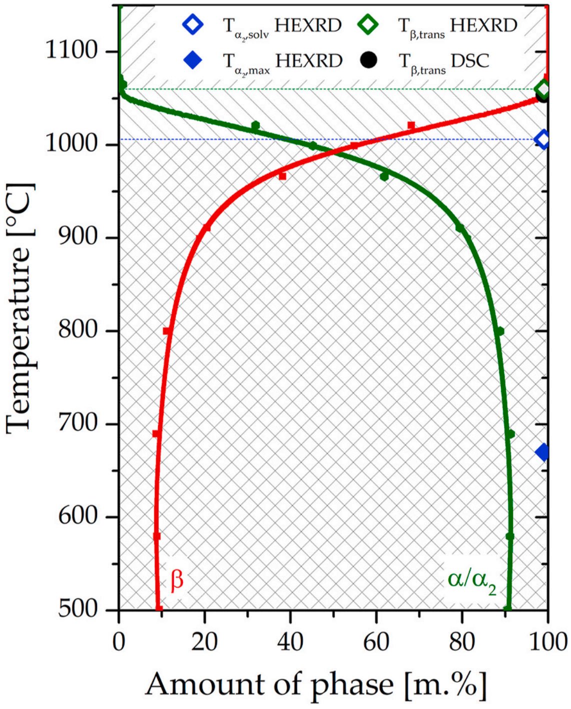

Fig. 7. DP of the [0001] zone axis of the α phase: a) Ti6242S and b) Ti6242S + TNM 1150 °C, to show that superlattice reflections, that belong to the α_2 phase, are only present in the Ti6242S + TNM 1150 °C variant.

3.5. Mechanical testing

The samples in as-SPS condition were further investigated by evaluating their mechanical properties. At first, tensile tests were carried out at different temperatures. As a result, the yield strength at an offset of 0.2% plastic strain and the plastic strain to fracture were evaluated for each tensile test specimen shown in Fig. 9a and Fig. 9b, respectively. Decker et al. [32] already reported that the addition of 10 m.% of TNM powder particles to the Ti6242S matrix leads to enhancement of the yield strength throughout the entire tested temperature range when compared to pure Ti6242S, see Fig. 9a. Comparing the yield strength of Ti6242S + TNM blends with partially and completely dissolved particles, no difference can be seen. The addition of 1 m.% B shows an increase in yield strength of almost 100 MPa when compared to the Ti6242S + TNM variants. This can be seen up to 550 °C. Above, grain boundary sliding becomes dominant in the fine-grained microstructure of the B-containing variant (Fig. 1b) and the curve drops sharply. Concurrently, the plastic strain to fracture increases from 2% at RT to above 40% at 650 °C because of the just mentioned grain boundary sliding. The sudden drop in the yield strength of the B reinforced variant above 550 °C, however, cannot be seen in the TNM containing variants.

In addition, in the present study creep tests were conducted at 600 °C under an applied load of 210 MPa on all variants in as-SPS condition. The resulting creep strain (ε) as a function of time is shown in Fig. 10. Crosses mark the position of the minimum creep rate ($\dot{\varepsilon}_{min}$) for each curve, and the value of $\dot{\varepsilon}_{min}$ is given next to the corresponding curve. The benchmark forms the Ti6242S in as-SPS condition reaching an $\dot{\varepsilon}_{min}$ of $5.0 \cdot 10^{-8}\ s^{-1}$ after 60 h. On the one hand, the fine-grained B containing variant, which shows the best tensile properties up to 550 °C because of the small grain size, has the highest $\dot{\varepsilon}_{min}$ and thus reaches $\varepsilon > 1\%$ creep strain already after 20 h under the applied load. On the other hand, the addition of TNM powder particles into the Ti6242S matrix improves the creep performance. In case of Ti6242S + TNM 1100 °C, $\dot{\varepsilon}_{min}$ is significantly decreased to $2.0 \cdot 10^{-8}\ s^{-1}$ after 115 h, resulting in a creep strain below 1% after 100 h under the applied load. The highest creep resistance is achieved for the Ti6242S + TNM 1150 °C variant with dissolved TNM where $\dot{\varepsilon}_{min}$ of $1.4 \cdot 10^{-8}\ s^{-1}$ is reached after 170 h.

4. Discussion

The technique of SPS is capable of producing dense near-α Ti-base alloys and their composites. All samples investigated in this study are in as-SPS condition (the process parameters are shown in Table 2), which is a suitable state to allow the comparison of the different samples, due to equal cooling rates. The Ti6242S sample with a lamellar α/β microstructure in as-SPS condition, as shown in Fig. 1a, contains coarse α colonies. This microstructure forms during moderate cooling from the β single phase field region ($T_{\beta,trans} = 1006 \pm 5$ °C) and exhibits excellent mechanical properties which we consider to be the benchmark. This is confirmed by the tensile tests provided by Decker et al. [32] for Ti6242S in as-SPS condition, which show similar yield strength and elongation values similar to other published data for Ti6242S [29], Ti6242 [2,47]

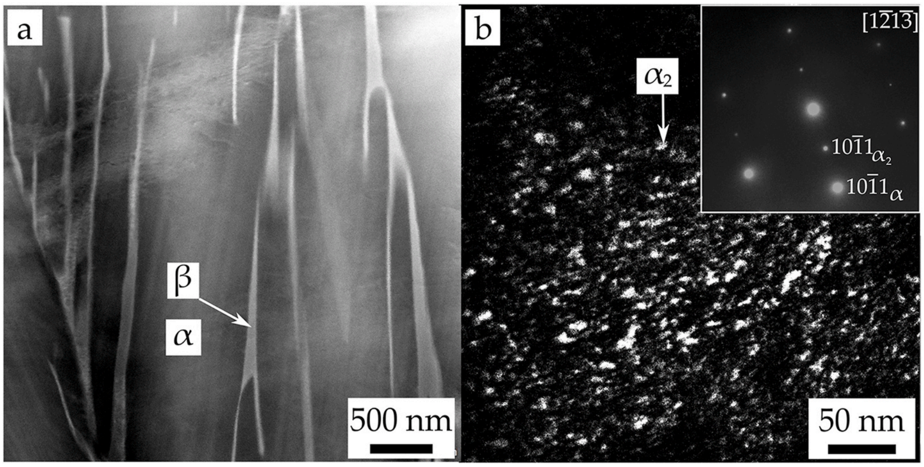

Fig. 8. a) TEM investigation of the Ti6242S + TNM 1150 °C sample in as-SPS condition. DF STEM image of α/β colonies, where the dark α lamellae are separated by bright, retained β phase. b) DF image of an α lamella. The insert shows the corresponding $[1\bar{2}1\bar{3}]$ diffraction pattern of the selected area, which reveals a hexagonal structure as well as superlattice reflections. The $10\bar{1}1_{\alpha2}$ superlattice reflection was used for the DF image. This $10\bar{1}1_{\alpha2}$ DF image illuminates nanometer sized ordered α_2 domains separated by disordered α phase or anti-phase boundaries, which appears in dark contrast.

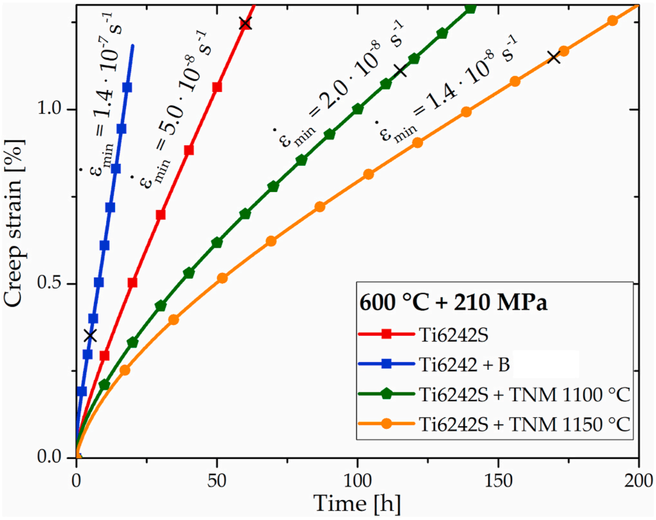

Fig. 9. a) The tensile test results show an enhanced yield strength for the B reinforced alloy variant up to 550 °C when compared to the values provided by Decker et al. [32]. At elevated temperatures, grain boundary sliding becomes dominant in the fine-grained B-containing variant, leading to a deteriorating yield strength but increasing fracture elongation, as shown in b).

or IMI834 (Ti-5.8Al–4Sn-3.5Zr-0.5Mo-0.7Nb-0.35Si-0.06C, m. %) [29]. Furthermore, the creep performance of Ti6242S in as-SPS condition as provided by the present study (Fig. 10), is in the same range as that derived for Ti6242S, produced via the casting route [2], demonstrating the potential of the SPS technique.

The addition of 1 m.% B to a Ti6242 alloy in this study yields high-melting titanium monoborides TiB, as identified by means of SEM, EDX and XRD. These needle-shaped borides are finely distributed in the matrix. The presence of borides leads to a drastic decrease in grain size (see Fig. 1b) due to heterogeneous nucleation. Furthermore, the microstructure changes to a non-lamellar one, which contains globular α phase surrounded by retained β phase, see Fig. 3. Grain boundary strengthening strongly affects the tensile properties. The TiB particles seem to provide only a minor strengthening contribution in the form of dispersoid strengthening according to Ref. [18,48–51], which can be split into two parts: Orowan strengthening and load transfer mechanism. The former is negligible due to the large size and inter-particle spacing of TiB, but the latter provides significant strengthening due to the amount of TiB with a high aspect ratio. As shown in Fig. 9, the yield strength could be increased to about 1100 MPa at RT for the TiB composite. This value exceeds the Ti6242S + TNM variants by about 100 MPa. An elongation to fracture of 1.7% could be maintained, despite the high amount of acicular brittle TiB. However, the strengthening effect of the fine α grain size gets lost at 600 °C due to grain boundary sliding [49], which appears at high temperatures for fine-grained microstructures and results in a drop of the yield strength and an increase in ductility. As a consequence, the creep resistance at 600 °C deteriorates, caused by

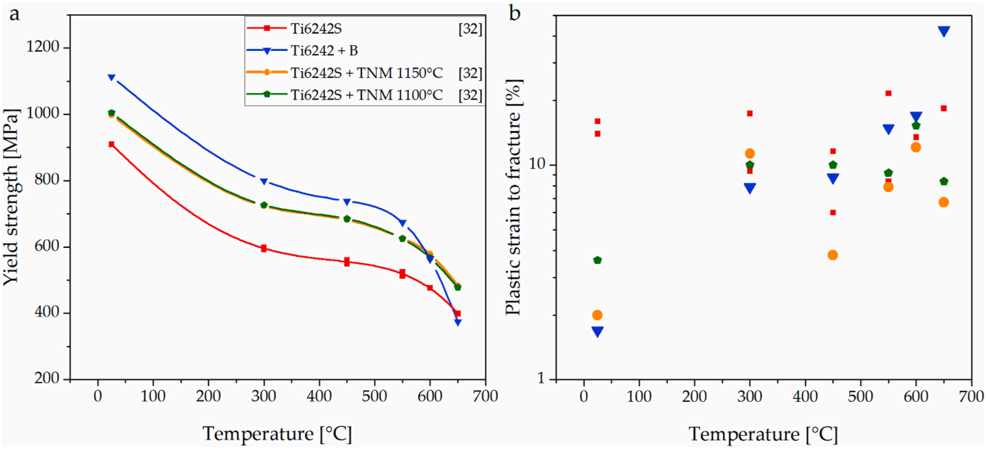

Fig. 10. Creep experiments are conducted at 600 °C under an applied load of 210 MPa for four different variants. Besides the creep curves, crosses on each curve mark the minimum creep strain rate, whose value is also given.

diffusion-controlled creep, which is pronounced for small grain sizes. Additionally, the B-reinforced variant contains no Si to form silicides, that would further improve the high-temperature properties [1].

Decker et al. [32] started mixing different amounts of TNM powder with Ti6242S, achieving an increase in yield strength. The Ti6242S variants with 10 m.% TNM particles (<20 µm particle size) and spark plasma sintering at 1100 °C or 1150 °C show an increase in yield strength of about 100 MPa compared to the benchmark Ti6242S sample and simultaneously maintain a fracture elongation above 2%, see Fig. 9. In the present study, creep experiments were conducted on these Ti6242S + TNM variants, which reveal the improvement of the creep resistance, i.e. a decrease in $\dot{\varepsilon}_{min}$ by half a magnitude. Consequently, 1% creep strain is still not reached after 100 h at 600 °C under the applied load of 210 MPa, as shown in Fig. 10. Regarding the tensile and creep results, the activated strengthening mechanisms have an effect up to 600 °C, no matter whether the TNM particles are dissolved in the Ti6242S matrix (SPS at 1150 °C) or not (SPS at 1100 °C). Therefore, it is concluded that there is no composite effect, but rather one that is traceable to the refinement of the microstructure and a change in the chemical composition. The refinement of the α colonies, and hence the reduction in the effective length for dislocation slip, is controlled by heterogeneous nucleation at the TNM particles during cooling, e.g. during transformation of β into α. Partial heterogeneous nucleation at the TNM particles is suggested by the absence of an α seam in Fig. 1c. Note, that the cooling rate, which is responsible for this α seam, stays roughly the same for all samples. As soon as the TNM particles are dissolved, grain growth of the β phase takes place, attributed to the lack of particles that effectively pin the β grain boundaries. Furthermore, the nucleation starts again exclusively at the parent β grain boundaries, confirmed by the α seam, as indicated in Fig. 1d. Consequently, slightly coarser grain structures are present in the Ti6242S + TNM 1150 °C variant when compared to the variant sintered at 1100 °C. Next to the α colonies, extended β grains appear at triple junctions of the TNM containing variants (see Fig. 2b and c). In general the large β grains would decrease the high-temperature strength [4], but the precipitation of α phase according to the Burgers orientation relationship again hardens it [4,52]. However, these small crossed α platelets could not be found in the retained β phase between the α lamellae of the α colonies (see Fig. 8a) as reported in Ref. [29,52]. Note that the adjustment of the lamellar spacing, which is almost equal for the three Ti6242S variants (see Fig. 2), is not crucial as the retained β phase in-between the parallel-oriented α lamellae easily enables the transfer of slip across the phase boundaries [4]. Therefore, it is concluded that the colony size is the major factor, which increases the strength of the TNM-containing variants by decreasing the effective length for dislocation slip.

An increase of 50 °C in the dwell temperature is enough to dissolve the TNM particles, which can still be identified at 1100 °C dwell temperature by employing SEM (see Fig. 2b). At a dwell temperature of 1150 °C, the TNM particles are dissolved homogeneously in the β matrix of the Ti6242S alloy. As a consequence of the change in the overall chemical composition, $T_{\beta,trans}$ increases to about 1060 °C, which is 60 °C above $T_{\beta,trans}$ of Ti6242S. Concurrently, the phase fractions at RT stay the same, i.e. 10 ± 2 m.% β and 90 ± 2 m.% α/α_2. However, due to the change in the chemical composition of the phases, additional strengthening mechanisms take place. The β phase exhibits an enrichment in Nb, shown in Table 3, leading to solid solution strengthening [4]. The majority phase α shows enrichment in Al, which leads to precipitation hardening by the formation of the intermetallic α_2-Ti_3Al phase smaller than 10 nm inside the α phase. Although the absolute amount of the α_2 phase could not be determined, its presence was confirmed by XRD (Fig. 4), HEXRD (Fig. 5) and TEM (Fig. 8). Furthermore, the in situ HEXRD experiment showed the α_2-maximum at 670 °C and $T_{\alpha 2,solv}$ at 1005 °C, thus about 355 °C above $T_{\alpha 2,solv}$ of the Ti6242S alloy [4,29]. The α_2 phase strengthens the Ti6242S + TNM variants at the expense of ductility. This behavior can be seen for the new Ti6242S + TNM alloy in the tensile results, presented in Fig. 9. Furthermore, the strengthening effect endures across the entire temperature range tested, seen by the parallel shift in the yield strength compared to the benchmark Ti6242S sample. The existence of α_2 benefits the creep resistance, as seen in Fig. 10. This proves the potential of the Ti6242S + TNM alloy for use at service temperatures up to 600 °C, which already exceed the maximum service temperature of 500 °C of Ti6242 [4], 540 °C of Ti6242S [28] and 550 °C of IMI834 [4].

The Ti6242S + 10 m.% TNM 1150 °C variant, where the TNM particles are completely dissolved and a chemical homogenization has taken place, represents a new alloy whose chemical composition can be determined by adding the mass fractions of the blend's components, as shown in Table 1. This newly manufactured alloy, Ti-8.3Al-1.8Sn-3.7Zr-2.0Mo-0.9Nb-0.08Si (m.%), represents a more ductile Ti–14Al–20Nb-3.2V–2Mo (m.%) variant at RT, which is called the Super Alpha 2 alloy with excellent high-temperature properties [53]. Moreover, the maximum service temperature of Ti–6Al-based alloys of around 550 °C is already surpassed by the newly developed alloy in as-SPS condition. Nevertheless, an adjustment of the microstructure by a subsequent heat treatment or thermomechanical treatment, based on the phase fraction diagram in Fig. 6, will further improve the mechanical properties of the new alloy, which is currently under investigation.

5. Summary

Spark plasma sintering was applied to generate new Ti-base alloys or composites with advanced mechanical properties up to 600 °C and is a straightforward tool to design new alloys or composites in a fast and independent manner on the basis of pre-alloyed powder.

The addition of B to the Ti6242 alloy improves the strength of the material by about 200 MPa at RT, when compared to the Ti6242S alloy, traceable mainly to the fine-grained globular α microstructure and, to a lesser extent, to a load transfer mechanism on the needle-shaped TiB. Here, the borides act as heterogeneous nucleation sites for the α transformation. The strength values of the Ti6242/TiB-MMC are always the highest compared to the other alloys investigated up to 550 °C. However, at higher temperatures the fine-grained structure deteriorates, which is also reflected in the creep results.

The Ti6242S + TNM blend sintered at 1100 °C forms a composite, where the TNM particles still appear in the microstructure, whereas when sintering at 1150 °C the TNM particles got entirely dissolved into the matrix and a new alloy was generated: Ti-8.3Al-1.8Sn-3.7Zr-2.0Mo-0.9Nb-0.08Si (m.%). The microstructures are lamellar and formed during cooling from the β single phase field region. The β grain size could be kept small in the Ti6242S + TNM variants due to grain boundary pinning by the TNM particles. When compared to the Ti6242S microstructure, the α colony size was refined due to the nucleation at the boundaries of the small β parent grains, confirmed by an α seam in the 1150 °C variant. The new Ti-8.3Al-1.8Sn-3.7Zr-2.0Mo-0.9Nb-0.08Si (m.%) alloy manufactured at 1150 °C from the Ti6242S + TNM blend enables the strengthening of the Al-enriched α phase by intermetallic α_2-Ti_3Al precipitates, which were identified by their superlattice reflections by means of (HE)XRD and TEM. Their domain size is estimated to be around 10 nm and they are completely stable up to 670 °C, which is essential for application. The Ti6242S + TNM variants show an equally improved tensile yield strength across the tested temperature range, but the newly developed Ti alloy exhibits a better performance during creep at 600 °C and 210 MPa. The outcomes prove that the strengthening is due to the refinement of the colonies as well as the alloying of additional elements rather than the presence of a metal matrix composite. Therefore, the high Al- and Nb-containing alloy further exceeds the service temperature limit of 550 °C established by Ti–6Al base alloys.

Declaration of competing interest

The authors declare that they have no known competing financial interests or personal relationships that could have appeared to influence the work reported in this paper.

CRediT authorship contribution statement

David Wimler: Conceptualization, Validation, Investigation, Writing - original draft. **Janny Lindemann:** Conceptualization, Investigation, Resources. **Christoph Gammer:** Investigation, Validation, Resources. **Petra Spoerk-Erdely:** Validation, Formal analysis. **Andreas Stark:** Investigation, Resources. **Helmut Clemens:** Conceptualization, Validation, Resources, Writing - review & editing, Supervision. **Svea Mayer:** Conceptualization, Validation, Resources, Writing - review & editing, Project administration, Supervision.

References

[1] C. Leyens, M. Peters, Titanium and Titanium Alloys: Fundamentals and Applications, Wiley-VCH, Weinheim, Chichester, 2003, 3527305343.

[2] D. Eylon, S. Fujishiro, F.H. Froes, Titanium alloys for high temperature applications — a review, High Temp. Mater. Process. 6 (1984) 1685, https://doi.org/10.1515/HTMP.1984.6.1-2.81.

[3] W. Sha, S. Malinov, Titanium Alloys: Modelling of Microstructure, Properties and Applications, Woodhead Pub, Cambridge, 2009, 9781439801482.

[4] G. Lütjering, J.C. Williams, Titanium, Springer, Berlin Heidelberg, 2013, 9783540713982.

[5] F.H. Froes, H. Friedrich, J. Kiese, D. Bergoint, Titanium in the family automobile: the cost challenge, J. Occup. Med. 56 (2004) 40–44, https://doi.org/10.1007/s11837-004-0144-0.

[6] B.P. Bewlay, S. Nag, A. Suzuki, M.J. Weimer, TiAl alloys in commercial aircraft engines, Mater. A. T. High. Temp. 33 (2016) 549–559, https://doi.org/10.1080/09603409.2016.1183068.

[7] S. Mayer, P. Erdely, F.D. Fischer, D. Holec, M. Kastenhuber, T. Klein, H. Clemens, Intermetallic β-Solidifying γ-TiAl based alloys – from fundamental research to application, Adv. Eng. Mater. 19 (2017), 1600735, https://doi.org/10.1002/adem.201600735.

[8] P. McQuay, Cast gamma TiAl alloys: are we there yet? in: K.J. Hemker (Ed.), Structural Intermetallics 2001: Proceedings of the Third International Symposium on Structural Intermetallic Minerals Metals & Materials Society, 2001, pp. 83–90. Warrendale, Pa. 0873395115.

[9] F. Appel, J.D.H. Paul, M. Oehring, Gamma Titanium Aluminide Alloys: Science and Technology, Wiley-VCH, Germany, 2012, 9783527315253.

[10] S. Mayer, M. Kastenhuber, H. Clemens, Advanced Titanium Aluminides - how to improve the creep resistance via compositional and microstructural optimization, Mater. Sci. Forum 941 (2018) 1484–1489. https://doi.org/10.4028/www.scientific.net/MSF.941.1484.

[11] S. Dadbakhsh, R. Mertens, L. Hao, J. van Humbeeck, J.-P. Kruth, Selective laser melting to manufacture "in situ" metal matrix composites: a review, Adv. Eng. Mater. 21 (2019), 1801244, https://doi.org/10.1002/adem.201801244.

[12] W.H. Yu, S.L. Sing, C.K. Chua, C.N. Kuo, X.L. Tian, Particle-reinforced metal matrix nanocomposites fabricated by selective laser melting: a state of the art review, Prog. Mater. Sci. 104 (2019) 330–379, https://doi.org/10.1016/j.pmatsci.2019.04.006.

[13] T. DebRoy, H.L. Wei, J.S. Zuback, T. Mukherjee, J.W. Elmer, J.O. Milewski, A. M. Beese, A. Wilson-Heid, A. De, W. Zhang, Additive manufacturing of metallic components – process, structure and properties, Prog. Mater. Sci. 92 (2018) 112–224, https://doi.org/10.1016/j.pmatsci.2017.10.001.

[14] S. Liu, Y.C. Shin, Additive manufacturing of Ti6Al4V alloy: a review, Mater. Des. 164 (2019), 107552, https://doi.org/10.1016/j.matdes.2018.107552.

[15] T. Voisin, J.-P. Monchoux, L. Durand, N. Karnatak, M. Thomas, A. Couret, An innovative way to produce γ-TiAl blades: spark Plasma Sintering, Adv. Eng. Mater. 17 (2015) 1408–1413, https://doi.org/10.1002/adem.201500019.

[16] P. Cavaliere, Spark Plasma Sintering of Materials: Advances in Processing and Applications, Springer International Publishing, 2019, 9783030053277.

[17] W. Lu, Di Zhang, X. Zhang, Y. Bian, R. Wu, T. Sakata, H. Mori, Microstructure and tensile properties of in situ synthesized (TiBw + TiCp)/Ti6242 composites, J. Mater. Sci. 36 (2001) 3707–3714, https://doi.org/10.1023/A:1017917631855.

[18] X. Guo, L. Wang, M. Wang, J. Qin, Di Zhang, W. Lu, Effects of degree of deformation on the microstructure, mechanical properties and texture of hybrid-reinforced titanium matrix composites, Acta Mater. 60 (2012) 2656–2667, https://doi.org/10.1016/j.actamat.2012.01.032.

[19] X. Tao, Z. Yao, S. Zhang, Reconstruction and refinement of TiB whiskers in titanium matrix composite after electron beam remelting, Mater. Lett. 225 (2018) 13–16, https://doi.org/10.1016/j.matlet.2018.04.099.

[20] A. Popov, N. Rossina, M. Popova, The effect of alloying on the ordering processes in near-alpha titanium alloys, Mater. Sci. Eng., A 564 (2013) 284–287, https://doi.org/10.1016/j.msea.2012.11.043.

[21] H.T. Tsang, C.G. Chao, C.Y. Ma, Effects of volume fraction of reinforcement on tensile and creep properties of in-situ MMC, Scripta Mater. 37 (1997) 1359–1365, https://doi.org/10.1016/S1359-6462(97)00251-0.

[22] T. Wang, B. Li, Z. Wang, Z. Nie, A microstructure with improved thermal stability and creep resistance in a novel near-alpha titanium alloy, Mater. Sci. Eng., A 731 (2018) 12–20, https://doi.org/10.1016/j.msea.2018.06.034.

[23] M. Ozerov, M. Klimova, A. Kolesnikov, N. Stepanov, S. Zherebtsov, Deformation behavior and microstructure evolution of a Ti/TiB metal-matrix composite during high-temperature compression tests, Mater. Des. 112 (2016) 17–26, https://doi.org/10.1016/j.matdes.2016.09.051.

[24] T. Saito, The automotive application of discontinuously reinforced TiB-Ti composites, J. Occup. Med. 56 (2004) 33–36, https://doi.org/10.1007/s11837-004-0125-3.

[25] H.M. Flower, P.R. Swann, D.R.F. West, Silicide precipitation in the Ti–Zr–Al–Si system, Metall. Mater. Trans. B 2 (1971) 3289–3297, https://doi.org/10.1007/BF02811609.

[26] S. Syngellakis, J.J. Connor (Eds.), Advanced Methods and Technologies in Metallurgy in Russia, Springer International Publishing, Cham, 2018, 9783319663531.

[27] W. Jia, W. Zeng, H. Yu, Effect of aging on the tensile properties and microstructures of a near-alpha titanium alloy, Mater. Des. 58 (2014) 108–115, https://doi.org/10.1016/j.matdes.2014.01.063.

[28] Titanium Metals Corporation, Timet - Datasheets, 2020. https://www.timet.com/assets/local/documents/datasheets/alphaalloys/6242.pdf. (Accessed 17 March 2020).

[29] G. Lütjering, Influence of processing on microstructure and mechanical properties of (α+β) titanium alloys, Mater. Sci. Eng., A 243 (1998) 32–45, https://doi.org/10.1016/S0921-5093(97)00778-8.

[30] W.G. Burgers, On the process of transition of the cubic-body-centered modification into the hexagonal-close-packed modification of zirconium, Physica 1 (1934) 561–586, https://doi.org/10.1016/S0031-8914(34)80244-3.

[31] C. Wei, X. Ma, X. Yang, M. Zhou, C. Wang, Y. Zheng, W. Zhang, Z. Li, Microstructural and property evolution of Ti6Al4V powders with the number of usage in additive manufacturing by electron beam melting, Mater. Lett. 221 (2018) 111–114, https://doi.org/10.1016/j.matlet.2018.03.124.

[32] S. Decker, J. Lindemann, L. Krüger, Metal matrix composites based on Ti-6242 synthesized by spark plasma sintering, Mater. Sci. Eng., A 732 (2018) 35–40, https://doi.org/10.1016/j.msea.2018.06.103.

[33] S. Decker, J. Lindemann, L. Krüger, Synthesis and mechanical properties of TiAl particle reinforced Ti-6Al-4V, Mater. Sci. Eng., A 674 (2016) 361–365, https://doi.org/10.1016/j.msea.2016.08.011.

[34] T. Voisin, L. Durand, N. Karnatak, S. Le Gallet, M. Thomas, Y. Le Berre, J.-F. Castagné, A. Couret, Temperature control during spark plasma sintering and application to up-scaling and complex shaping, J. Mater. Process. Technol. 213 (2013) 269–278, https://doi.org/10.1016/j.jmatprotec.2012.09.023.

[35] G. Petzow, Metallographisches, Keramographisches, Plastographisches Ätzen, sixth ed., Borntraeger-Verlag, Berlin, 1994, 9783443230142.

[36] L.B. McCusker, R.B.V. Dreele, D.E. Cox, D. Louër, P. Scardi, Rietveld refinement guidelines, J. Appl. Crystallogr. 32 (1999) 36–50, https://doi.org/10.1107/S0021889898009856.

[37] N. Schell, R.V. Martins, F. Beckmann, H.U. Ruhnau, R. Kiehn, A. Schreyer, The high energy materials science beamline at PETRA III, in: Stress Evaluation in Materials Using Neutrons and Synchrotron Radiation, Trans Tech, Stafa-Zurich, United Kingdom, 2008, pp. 261–266. https://doi.org/10.4028/www.scientific.net/MSF.571-572.261.

[38] A.P. Hammersley, S.O. Svensson, M. Hanfland, A.N. Fitch, D. Hausermann, Two-dimensional detector software: from real detector to idealised image or two-theta scan, High Pres. Res. 14 (1996) 235–248, https://doi.org/10.1080/08957959608201408.

[39] T. Schmoelzer, K.-D. Liss, P. Staron, S. Mayer, H. Clemens, The contribution of high-energy X-rays and neutrons to characterization and development of intermetallic titanium Aluminides, Adv. Eng. Mater. 13 (2011) 685–699, https://doi.org/10.1002/adem.201000296.

[40] L. Spieß, G. Teichert, R. Schwarzer, H. Behnken, C. Genzel, Moderne Röntgenbeugung: Röntgendiffraktometrie für Materialwissenschaftler, Physiker und Chemiker, second., überarbeitete und erweiterte Auflage, Vieweg+Teubner Verlag/GWV Fachverlage GmbH Wiesbaden, Wiesbaden, 2009, 9783835101661.

[41] R.M. Imayev, V.M. Imayev, M. Oehring, F. Appel, Alloy design concepts for refined gamma titanium aluminide based alloys, Intermetallics 15 (2007) 451–460, https://doi.org/10.1016/j.intermet.2006.05.003.

[42] W. Wallgram, T. Schmölzer, L. Cha, G. Das, V. Güther, H. Clemens, Technology and mechanical properties of advanced γ-TiAl based alloys, Int. J. Mater. Res. 100 (2009) 1021–1030, https://doi.org/10.3139/146.110154.

[43] M. Kastenhuber, T. Klein, B. Rashkova, I. Weißensteiner, H. Clemens, S. Mayer, Phase transformations in a β-solidifying γ-TiAl based alloy during rapid solidification, Intermetallics 91 (2017) 100–109, https://doi.org/10.1016/j.intermet.2017.08.017.

[44] S. Cao, C.V.S. Lim, B. Hinton, X. Wu, Effects of microtexture and Ti_3Al (α_2) precipitates on stress-corrosion cracking properties of a Ti-8Al-1Mo-1V alloy, Corrosion Sci. 116 (2017) 22–33, https://doi.org/10.1016/j.corsci.2016.12.012.

[45] P. Samimi, I. Ghamarian, D. Brice, M.J. Kaufman, P.C. Collins, On the influence of compositional variations on the oxidation performance and oxygen-induced phase transformations in Ti-based systems, in: V. Venkatesh, A.L. Pilchak, J.E. Allison, S. Ankem, R. Boyer, J. Christodoulou, H.L. Fraser, M.A. Imam, Y. Kosaka, H. J. Rack, A. Chatterjee, A. Woodfield (Eds.), Proceedings of the 13th World Conference on Titanium: Sponsored by Titanium Committee of the Structural Materials Division of the Minerals, Metals & Materials Society (TMS), Held August 16-20, 2015, Wiley, Hoboken, New Jersey, 2016, pp. 1521–1526, https://doi.org/10.1002/9781119296126.ch255. Manchester Grand Hyatt, San Diego, California, USA.

[46] P.D. Nellist, S.J. Pennycook, The principles and interpretation of annular dark-field Z-contrast imaging, in: P.W. Hawkes (Ed.), Advances in Imaging and Electron

Physics, Academic Press, San Diego, San Francisco, 2000, pp. 147–203, https://doi.org/10.1016/S1076-5670(00)80013-0.

[47] J.R. Davis, Properties and Selection: Nonferrous Alloys and Special-Purpose Materials, [tenth. ed.], Sixth, ASM International, Materials Park, Ohio, 2000, 0871703785 print.

[48] S. Wei, L. Huang, X. Li, Y. Jiao, W. Ren, L. Geng, Network-strengthened Ti-6Al-4V/(TiC+TiB) composites: powder metallurgy processing and enhanced tensile properties at elevated temperatures, Metall. Mater. Trans. 50 (2019) 3629–3645, https://doi.org/10.1007/s11661-019-05244-7.

[49] R.W. Cahn, P. Haasen, Physical Metallurgy, Fourthth, Rev. And Enhanced, ed., North-Holland, Amsterdam, New York, 2010, 9780444898753.

[50] F. Saba, F. Zhang, S. Liu, T. Liu, Reinforcement size dependence of mechanical properties and strengthening mechanisms in diamond reinforced titanium metal matrix composites, Compos. B Eng. 167 (2019) 7–19, https://doi.org/10.1016/j.compositesb.2018.12.014.

[51] T.W. Clyne, P.J. Withers, An Introduction to Metal Matrix Composites, first. paperback ed., Cambridge Univ. Press, Cambridge, 1995, 0521418089.

[52] Y. Chong, N. Tsuji, T. Bhattacharjee, Investigation on the Bi-lamellar microstructure in Ti-6Al-4V, in: V. Venkatesh, A.L. Pilchak, J.E. Allison, S. Ankem, R. Boyer, J. Christodoulou, H.L. Fraser, M.A. Imam, Y. Kosaka, H.J. Rack, A. Chatterjee, A. Woodfield (Eds.), Proceedings of the 13th World Conference on Titanium: Sponsored by Titanium Committee of the Structural Materials Division of the Minerals, Metals & Materials Society (TMS), Held August 16-20, 2015, Wiley, Manchester Grand Hyatt, San Diego, California, USA, 2016, pp. 663–667, https://doi.org/10.1002/9781119296126.ch110. Hoboken, New Jersey.

[53] G. Proske, G. Lütjering, J. Albrecht, D. Helm, M. Daeubler, The microstructure and mechanical properties of the intermetallic compound Super Alpha 2, in: C.T. Liu, D. P. Pope, S.-H. Whang (Eds.), High Temperature Aluminides and Intermetallics: Proceedings of the Second International ASM Conference on High Temperature Aluminides and Intermetallics, September 16-19, 1991, Elsevier, San Diego, CA, USA, 1992, pp. 310–316, https://doi.org/10.1016/B978-1-85166-822-9.50051-0. London.